J. COMBIN. MATH. COMBIN. COMPUT. 127b (2025) 5809--5829

Journal of Combinatorial Mathematics and Combinatorial Computing
www.combinatorialpress.com/jcmcc

Combinatorial Press

Computational and Risk Assessment Modeling of Bridge Inspection Data Enabled by Sensors and Monitoring Systems

Yunfeng Xu[1,✉], Chengfeng Tang[2], Jinhua Chen[3]

[1] *School of Civil Engineering, Chongqing Jiaotong University, Chongqing, 400074, China*

[2] *School of Architecture and Engineering, Xinjiang University, Urumqi, Xinjiang, 830017, China*

[3] *School of Materials Science and Engineering, Chongqing University of Technology, Chongqing, 400074, China*

ABSTRACT

Aiming at the bridge monitoring system, some of the monitoring data are abnormal due to equipment failure and environmental impacts. In this paper, the time-frequency domain convolutional neural network method is applied to the calculation of monitoring data and the risk assessment of bridge structure. The data collected by the acceleration sensor is firstly sliced and sampled and visualized. Then wavelet analysis is used to preprocess the cluttered data, and Wigner-Ville distribution and Fast Fourier Transform are introduced to extract time-frequency features from the collected data. A convolutional neural network is proposed and the network is trained on dual channel images fusing time and frequency domain images. By analyzing the spectrogram and and time-frequency diagram of the bridge monitoring data, the method of this paper classifies the bridge health condition into three kinds: no disease, slight disease and disease, which can accurately determine the health condition of different bridges, and the assessment accuracy of the risk assessment model based on the fusion of time-frequency domain information reaches 97.78%, which indicates that the high efficiency and feasibility of the bridge inspection data computation and the risk assessment model in this paper can meet the actual engineering construction needs of bridge inspection.

Keywords: Wigner-Ville distribution, Fast Fourier transform, Wavelet analysis, Convolutional neural network, Bridge inspection

1. Introduction

Bridges, as throat projects, are important channels and driving forces for urban development and have a significant impact on urban development [1-2]. However, with the rapid development of China's

✉ Corresponding author.
E-mail address: 13527516308@163.com (Y. Xu).

Received 10 January 2024; Revised 15 February 2024; Accepted 25 December 2024; Published Online 16 April 2025.
DOI: 10.61091/jcmcc127b-320

economy and transportation industry, the number of vehicles grows, and various natural disasters and man-made damages, such as overloading and impact, greatly accelerate the damage and aging of these bridge structures, which makes the bridge safety problems increasingly prominent [3-6]. In addition, how to realize the safety monitoring of bridges and assess their existing risks has become the focus of attention of the academic and engineering communities at home and abroad [7-8].

Both the inspection and assessment of bridges are important work, through which the problems existing in bridges can be effectively found and solved, providing scientific basis for the repair and reinforcement of bridges, as well as providing guarantee for the safety and smoothness of transportation [9-12]. The ways of bridge inspection are more diversified, with visualization inspection, non-destructive inspection and destructive inspection [13-14]. Among them, visualization inspection is the most common and the most basic one, and sensors and bridge health monitoring systems are widely used as an important part of visualization [15-17]. Sensor is a comprehensive technical discipline that uses various functional materials to realize information detection, which is one of the basic technologies to realize informationization [18-19].

The rapid development of modern measurement, control and automation technology, especially the development of electronic information science, has greatly promoted the development of modern sensor technology, which has become an indispensable link in detecting bridge data [20-22]. And the bridge health monitoring system by arranging all kinds of sensors on the bridge, sensing all kinds of information, and through the wired or wireless way back to the rear computer, in the obtained massive monitoring data, data processing and analysis of the bridge safety operation is of great significance [23-26]. Timely processing and analyzing the monitoring data, discovering the intrinsic connection between the data as well as the bridge structural information contained, converting the monitoring signals into state information that can be used to assess the structural state, thus conducting safety assessment and providing guidance for the bridge management and maintenance units [27-30].

In this paper, a large-span cable-stayed bridge in China is taken as the research object, and the data collected by several acceleration sensors of the bridge are visualized and divided, and the wavelet analysis method is used for noise reduction and preprocessing of the cluttered data. Then the signal data were subjected to Wigner-Ville processing and Fast Fourier Transform respectively, in order to obtain the energy distribution of the signal frequency and the periodic characteristics of the coordinate timing of the bridge data. Then a risk assessment strategy for bridge inspection data based on convolutional neural network and time-frequency domain information fusion is introduced. The original time series is transformed into an image representation at both time and frequency domain levels, and then a channel image containing dual information in the time-frequency domain and manually labeled information is designed, and the convolutional neural network model of this paper is constructed on this image data. Finally, the model designed in this paper is used for health detection and risk assessment of bridge inspection data to verify the performance of the model.

2. Bridge inspection data calculation and risk assessment modeling

2.1. *Preparation of the data set*

The bridge health monitoring data in this paper comes from the acceleration data of the health monitoring system of a large-span cable-stayed bridge in China, and the length of data collection is one month. The bridge has a main span of 1080 m, side spans of 300 m, and a tower height of 300 m, in which a total of 30 accelerometers installed on the deck and tower collect and store the bridge acceleration information with a sampling frequency of 20 Hz.

The data collected by each accelerometer in one month are sliced with a slicing interval of 1h and a single sample dimension of 1×72000.The data of each sample are divided by time domain image type and given labels. Among them: the time domain image shows the level of the central axis, and the normal fluctuation of the curve is labeled as normal. Most of the blank areas of the time-domain image are labeled as missing, and the main reasons for the missing abnormality are the failure of the sensor array equipment and the breakage of the data transmission cable. The jagged time domain image is labeled as sub-minor value, which is usually caused by the sensor's own failure, damage or environmental factors. Time domain image contains one or more mutations, vibration curve features are greatly scaled marked as outliers, outliers caused by the main reason for the sensor current instantaneous increase or monitoring system electromagnetic interference. A square shape in the time-domain image of the data due to unstable voltage supply to the sensor array is labeled as over-range oscillation. A monotonous rise/fall in the time domain image is labeled as a trend. The time domain image with localized monotonous rise/fall alternately is marked as drift.

2.1.1. Data visualization. In this paper, the time-frequency analysis method is used to visualize the bridge acceleration data, extract the joint time-frequency features, transform the one-dimensional acceleration data into two-dimensional time-frequency images, and prepare the image dataset for the input and training of the model. The time-frequency analysis method mainly includes short-time Fourier transform and continuous wavelet transform.

The short-time Fourier transform needs to adjust the size of the window function according to the specific characteristics of the target data to achieve the ideal analysis effect. The bridge acceleration signal is characterized by randomness, and the fixed-window short-time Fourier transform has poor adaptability to non-smooth signals, and is unable to analyze the data with multiple features at the same time, and the feature extraction effect of the sample of the data set is not ideal. Continuous wavelet transform can shift and scale the wavelet function according to the different signal frequencies, transform the window size according to the signal characteristics while ensuring that the window area remains unchanged, thus amplifying the local characteristics of the signal, which has stronger adaptability to non-smooth signals and better analytical effect, so the article adopts the continuous wavelet transform method to analyze the data in terms of time-frequency analysis and feature extraction.

2.1.2. Data set partitioning. Randomly selected samples from the preprocessed time-frequency image database are proportionally divided into training, validation and test sets, with the ratio of each part being 6:2:2. The network model weight parameters are updated and optimized through the training and validation sets. The unused test set will be used to test the accuracy and generalization ability of the model after completing the training.

2.2. Wavelet analysis

2.2.1. Basic wavelet theory. Wavelet analysis is a representative result of the development of harmonic analysis technology in mathematics, which has a complete mathematical theoretical foundation and important application value. Wavelet analysis as a time-frequency domain analysis method is the development of frequency domain analysis methods. The traditional Fourier analysis [31] makes a direct definition $\psi(t) \in L^2(R)$ for a smooth signal, where $\psi(t)$ is a function with finite energy and $L^2(R)$ is expressed as a square-productible real number space. When the Fourier transform $\Psi(\omega)$ of $\psi(t)$ satisfies the tolerance condition:

$$C_\psi = \int_R \frac{|\Psi(\omega)|^2}{|\omega|} d\omega < \infty \tag{1}$$

Then $\psi(t)$ is said to be a fundamental wavelet or wavelet mother function. In the tolerance condition or complete reconstruction condition for wavelets, $\psi(t)$ is a continuous function, yet $|\omega| \neq 0$ on the denominator. When $\omega = 0$, based on the tolerance condition can be obtained:

$$W(0)=0 \to \int_{-\infty}^{+\infty} \psi(t) e^{-i\omega t} dt = \int_{-\infty}^{+\infty} \psi(t) dt = 0 \tag{2}$$

That is, the wavelet mother function satisfies an integral of 0 in the time domain.

The wavelet function has significant characteristics. The word “small” in wavelet refers to the rapid decay of the wavelet parent function. The “wave” is the expression of its volatility. From the mathematical point of view, the DC component of the wavelet function is 0, and because of the energy signal characteristics of $\psi(t)$, it can be deduced that the wavelet function is characterized by oscillation near the origin, and away from the origin converges to the horizontal coordinate axis. In the time domain, the wavelet has good time localization ability, i.e., the signal amplitude rapidly decays to 0 after a short fluctuation, while in the frequency domain, the wavelet shows band-pass characteristics, and the signal energy is concentrated near the center frequency.

In principle, the function that satisfies the tolerance condition can be used as the wavelet mother function $\psi(t)$. The wavelet basis function can be obtained by stretching and translating the wavelet parent function:

$$\psi_{a,b}(t) = \frac{1}{\sqrt{|a|}} \psi(\frac{t-b}{a}) \tag{3}$$

Where $\psi_{a,b}$ is the wavelet basis, i.e., the wavelet function family, a is the scale factor, b is the time factor ($a,b \in R$ and $a \neq 0$), and $|a|^{-0.5}$ is the normalization constant. By introducing the normalization constants, the total energy of the wavelet bases is kept constant at different scale factors to achieve the “normalization” of the wavelet bases.

$$\| \psi_{a,b} \|^2 = \int_{-\infty}^{+\infty} | \frac{1}{\sqrt{|a|}} \psi(\frac{t-b}{a}) |^2 \, dt = \int_{-\infty}^{+\infty} | \psi(\frac{t-b}{a}) |^2 d(\frac{t}{a}) = \int_{-\infty}^{+\infty} | \psi(t) |^2 dt \tag{4}$$

The Fourier transform of the wavelet mother function $\psi(t)$ is:

$$\Psi_{a,b}(\omega) = \frac{1}{\sqrt{|a|}} \int_{-\infty}^{+\infty} \psi(\frac{t-b}{a}) e^{-i\omega t} dt = \frac{a}{\sqrt{|a|}} e^{-i\omega t} \Psi(a\omega) \tag{5}$$

Denote the center and window width of the wavelet mother function $\psi(t)$ and its Fourier transform $\Psi(\omega)$ as $E(\psi)$ and $\Delta(\psi)$ and $E(\Psi)$ and $\Delta(\Psi)$, respectively. Then it is deduced that the center as well as the bandwidth of $\psi_{a,b}(t)$ and $\Psi_{a,b}(\omega)$ are:

$$\begin{cases} E(\psi_{a,b}) = b + aE(\psi) \\ \Delta(\psi_{a,b}) = |a| \Delta(\psi) \end{cases} \tag{6}$$

$$\begin{cases} E(\Psi_{a,b}) = \dfrac{E(\Psi)}{a} \\ \Delta(\Psi_{a,b}) = \dfrac{\Delta(\Psi)}{|a|} \end{cases} \tag{7}$$

Due to the frequency domain bandpass characteristics of wavelets, the wavelet parent function can cover a smaller bandwidth. And after the wavelet is transformed by stretching and translation, the narrowband signal of a single wavelet is transformed into a wavelet basis that can cover a wider bandwidth.

2.2.2. Continuous wavelet transform. The wavelet transform is an integral transform in which the wavelet basis function $\psi(t)$, called the mother wavelet, is convolved with the signal $f(t)$ to be analyzed to obtain the wavelet coefficients. For any energy limited signal $f(t) \in L^2(R)$, its continuous wavelet transform (CWT) [32] is expressed as:

$$W(a,b)=\langle f(t),\psi_{a,b}(t)\rangle=\frac{1}{\sqrt{|a|}}\int_{-\infty}^{+\infty}f(t)\psi^*(\frac{t-b}{a})dt \tag{8}$$

where $W(a,b)$ is a number of wavelet coefficients obtained by decomposing the signal $f(t)$ and ψ^* is denoted as the complex conjugate of the wavelet function $\psi(t)$.

For the time and frequency domain ranges of the wavelet transform on a single scale, the time and frequency windows of the continuous wavelet can be deduced as:

$$\begin{gathered}[b+aE(\psi)-|a|\Delta(\psi),b+aE(\psi)+|a|\Delta(\psi)]\\ \left[\frac{E(\Psi)}{a}-\frac{\Delta(\Psi)}{|a|},\frac{E(\Psi)}{a}+\frac{\Delta(\Psi)}{|a|}\right]\end{gathered} \tag{9}$$

The time-frequency window of a continuous wavelet $\psi_{a,b}(t)$ is a rectangle in the time-frequency plane that varies with the scale factor a. As a becomes progressively larger, the time window of the wavelet becomes wider, the frequency window becomes narrower, and the dominant frequency is reduced to match the low-frequency component. When a becomes gradually smaller, the wavelet's time window becomes narrower, the frequency window becomes wider, and the dominant frequency is raised to match the high-frequency component. This variation of the wavelet basis $\psi_{a,b}$ with the scale factor a gives the wavelet the ability to focus the spectrum. Calculate the area of the time-frequency window:

$$\begin{gathered}\left[b+aE(\psi)-|a|\Delta(\psi),b+aE(\psi)+|a|\Delta(\psi)\right]\\ \times\left[\frac{E(\Psi)}{a}-\frac{\Delta(\Psi)}{|a|},\frac{E(\Psi)}{a}+\frac{\Delta(\Psi)}{|a|}\right]=4\Delta(\psi)\Delta(\Psi)\end{gathered} \tag{10}$$

It is only related to the wavelet mother function and not to the scale factor a and the time factor b. This adaptive feature endows wavelets with the ability of time-frequency localization for non-smooth signals. Therefore, wavelet analysis methods are also called time-frequency analysis methods.

Based on the tolerance conditions, the wavelet coefficients obtained from the continuous wavelet transform can also be inverted to compute the original signal. The reconstruction of the signal $f(t)$ is realized by using the dual integration of the wavelet coefficients with the reconstruction expression:

$$f(t)=\frac{1}{\pi C_\psi}\int_{-\infty}^{+\infty}\int_{-\infty}^{+\infty}\frac{1}{a^2}W(a,b)\psi(\frac{t-b}{a})\frac{da}{\sqrt{|a|}}db \tag{11}$$

Continuity in continuous wavelet transform refers to the continuity of time t, scale factor a and time factor b. Continuity enables the wavelet transform to obtain good analytical accuracy. However, the opposite continuity also brings difficulties in its computation. The wavelet reconstruction expression is a decomposition of the signal $f(t)$ on the basis $\psi_{a,b}(t)$, and the computed wavelet coefficients $W(a,b)$ are the coordinates of the signal on this set of bases. From a linear algebra point of view, the continuously varying parameter scale factor a and time factor b in the continuous wavelet transform leads to the existence of a linear correlation of the wavelet coefficient $W(a,b)$ matrix. This represents the existence of information redundancy in the continuous wavelet transform, which can be eliminated by constructing orthogonal basis functions.

2.3. Wigner-Ville distribution

Time-frequency analysis is a class of research methods for describing the spectral components of a signal over time, which describes the energy or density of the signal at both time and frequency in some way, with the ultimate goal of creating a distribution that can represent the energy or intensity of the signal frequency over time.

The Wigner-Ville [33] distribution is an important theory for time-frequency analysis and has many excellent properties. For a signal $x(t)$, its Wigner-Ville distribution (WVD) is defined as:

$$WVD(t,\omega)=\frac{1}{2\pi}\int_{-\infty}^{+\infty}x(t+\frac{\tau}{2})x^{*}(t-\frac{\tau}{2})e^{-j\omega\tau}d\tau \tag{12}$$

The instantaneous correlation function of the signal $x(t)$ is expressed as:

$$r(t,\tau)=x(t-\frac{\tau}{2})x^{*}(t-\frac{\tau}{2}) \tag{13}$$

The WVD distribution of a signal $x(t)$ is the Fourier transform of its instantaneous correlation function $r(t,\tau)$.

It can also be expressed as:

$$WVD(t,\omega)=\frac{1}{2\pi}\int_{-\infty}^{\infty}r(t,r)e^{-j\omega\tau}d\tau \tag{14}$$

Integrating both sides of Eq. is then:

$$\begin{aligned}&\frac{1}{2\pi}\int_{-\infty}^{+\infty}WVD_{x}(t,\omega)dt\\&=\frac{1}{2\pi}\int\int x(t+\tau/2)x^{*}(t-\tau/2)e^{-j\omega\tau}d\tau dt\\&=\frac{1}{2\pi}\int\int x(t+\tau/2)x^{*}(t-\tau/2)d\tau.\frac{1}{2\pi}e^{-j\Omega\tau}d\Omega\\&=\frac{1}{2\pi}\int\int x(t+\tau/2)x^{*}(t-\tau/2)\delta(\tau)d\tau.\frac{1}{2\pi}\\&=|x(t)|^{2}\end{aligned} \tag{15}$$

The above calculation shows that one can obtain $WVD_x(t,\omega)$ integrating the frequency Ω in a certain frequency band, which results in the instantaneous energy of the signal at the moment t.

Let the Fourier transform of the signal $x(t)$ be $X(\omega)$, then the WVD distribution can also be expressed in terms of the spectrum of the analyzed signal as follows:

$$WVD(t,\omega)=\frac{1}{2\pi}\int_{-\infty}^{+\infty}X^{*}(\omega+\frac{v}{2})X(\omega-\frac{v}{2})e^{-jtv}dv \tag{16}$$

Integrate over time t simultaneously for both sides of Eq:

$$\begin{aligned}&\int_{-\infty}^{+\infty}WVD_{x}(t,\Omega)dt\\&=\frac{1}{2\pi}\iint X(\Omega+\theta/2)X^{*}(\Omega-\theta/2)e^{j\theta t}d\theta t\\&=\frac{1}{2\pi}\int X(\Omega+\theta/2)X^{*}(\Omega-\theta/2)\delta(\theta)d\theta\\&=|x(\Omega)|^{2}\end{aligned} \tag{17}$$

The above calculation shows that the WVD transform $WVD_x(t,\Omega)$ of the signal $x(t)$ integrates over the frequency t in a certain frequency band, and the result is the instantaneous energy of the signal at the Ω moment.

In summary, the analysis shows that the WVD transform is obtained by multiplying the signal of a certain time in the past by the signal of a certain time in the future, and then using the time difference as the independent variable to obtain the Fourier transform of the product of the two signals. It can be seen that WVD is not limited by the conflicting time-frequency accuracy in the short-time Fourier algorithm, maximizes the utilization of the whole time-domain signal, and has a high time-frequency focusing performance. For a single signal, WVD can accurately reflect the WVD distribution of single-frequency periodic signals in the two-dimensional domain as the signal energy changes with time and frequency.

2.4. Fast Fourier Transform

The Fourier transform is a research method used to analyze signals in the frequency domain, usually used to transform signals between the time domain and the frequency domain, and in which the transformation process is reversible and the energy remains constant. The essence of the Fourier transform is to decompose the data into the sum of sine and cosine signals of different periods, and then express the result of this decomposition into the frequency domain. By analyzing the coordinate time data converted to the frequency domain, it is easy to extract the different period signals contained in the data and to compare the overall intensity exhibited by the different period signals. For the function $f(t)$, its continuous Fourier transform and inverse transform are shown in the following equations:

$$F(w)=\int_{-\infty}^{+\infty} e^{-i\omega t} f(t)dt \tag{18}$$

$$f(t)=\frac{1}{2\pi}\int_{-\infty}^{+\infty} e^{i\omega t} F(w)dw \tag{19}$$

In practice, data of finite length is generally studied. The discrete Fourier transform (DFT) [34] can sample a finite length sequence with a finite number of discrete points. Let $x(n)$ be a set of data containing N discrete points, then its discrete Fourier transform is expressed as:

$$X(k)=\sum_{n=0}^{N-1} x(n)W_N^{kn}, k=0,1,2,\cdots,N-1 \tag{20}$$

$$W_N = e^{\frac{-2\pi i}{N}} \tag{21}$$

Scientists have improved the DFT and proposed the Fast Fourier Transform (FFT), which largely reduces the computational volume of the DFT and thus improves the computational efficiency. In this paper, the fast Fourier transform method is used to extract and analyze the periodic signals of coordinate time series.

2.5. Risk assessment methods based on time-frequency domain information fusion

2.5.1. Fusion of time-frequency domain information and data transformation. CNN is a deep learning algorithm that has demonstrated excellent performance in a number of domains such as image and speech recognition, especially in image recognition tasks. For building health inspection studies, CNNs are widely used for the recognition of surface defects and the confirmation of building safety images.

This chapter describes a computer vision approach that is inspired by manual troubleshooting data processing and simulates human visual understanding of images. To this end, the original monitoring time-series data are expressed in two dimensions, time domain and frequency domain, and image processing and image recognition techniques can be used to extract valuable information from this composite two-dimensional image expression space, and to understand and analyze the bridge monitoring data at a deeper level.

The first is the segmentation of the data, the original sequence of data points into many copies, so that it can be easier to deal with and in order to analyze the data of a particular interval. Then the segmented data is visualized. Then comes the image generation, where the data images in the time and frequency domains are extracted and these data images are stored as gray scale images. Next, each pair of time and frequency domain images is stacked so that a two-channel image is generated. The next step is image labeling, where the distinctive main features of both are considered when labeling the generated time-frequency domain composite image. The last step is model training, to construct a model based on convolutional neural network, and this model has a dual-channel input port, by training the classified anomalous data to learn the manifestation of anomalous data. The optimized CNN improves the generalization ability of the model, reduces the possibility of model overfitting, and improves the prediction accuracy of the model on bridge monitoring data.

2.5.2. Convolutional neural network based on time-frequency domain information. In this section, a CNN needs to be designed with the main framework and all the values. Then a time-frequency domain composite image x is set as the input to the neural network.

When performing convolutional layer processing, the basic step is to perform convolutional computation of the input layer and filters to generate the intermediate feature mapping map.

$$x_j^l = f\left(\sum_{i=1}^{l} x_i^{l-1} * F_{ij}^l + b_j^l\right), j \in [1, J] \tag{22}$$

In the expression, x_j^l represents the j channel element of the input layer l. F_{ij}^l represents the i channel element of the l layer filter j. b_j^l represents the bias of the l-layer filter j. l represents the number of $l-1$ channel layers. J represents the number of l channel layers. $f(\cdot)$ represents the activation function.

When performing image convolution, the filter slides along the input image and performs a term-by-term multiplication at each of its positions, a process called "receptive field". More specifically, the filter multiplies with the corresponding pixels in the receiving field of the input image and sums the results of the computation to obtain the pixel values at the corresponding positions in the feature map. Next, the filter moves to the next receiving field of the input image according to a preset step size and repeats the above process. The size of the step size determines how far the filter moves over the input image, and a larger step size reduces the size of the feature map. The size of the 2D output feature map is calculated by the following equation:

$$D_{out} = (D_{in} - C) / S_{conv} + 1 \tag{23}$$

In Eq. D_{in} is the edge length of the input layer x^{l-1}, C is the filter edge length, D_{out} is the edge length of the output layer x^{l-1}, and S_{conv} is the spanning in the direction of the height and width.

In each channel, subsampling is performed independently on the feature map, and the decision of its output values is taken by picking representative values within the received range of the input data. By downscaling the data while keeping the core features unchanged, the pooling layer is able to keep the feature map size reasonable while simplifying the network structure and reducing the computational burden. More notably, such features refined by the dimensionality reduction process remain surprisingly robust to subtle changes, rotations, and shifts. The output values are as follows:

$$x_j^l = x_i^{l-1} * P_j^l, i \in (1, l) \tag{24}$$

In the expression, x_j^l is the j channel element of the input layer l. P_j^l is the i-channel of the pooling operator of layer l. l is the number of channels in the $l-1$ and l layers.

The dimensional size of the in-plane feature map output can be calculated using the following mathematical formula:

$$D_{out} = (D_{in} - P_{pool}) / S_{pool} + 1 \tag{25}$$

In the expression, P_{pool} is the pooling operator edge length. S_{pool} is the in-plane height and width step.

Previous studies have commonly used average pooling for downsampling. However, recent findings point out that maximum pooling performs better as an operon. Consequently, in this study, the neural network classification unit was chosen to be composed of two main parts: the Softmax layer and the fully connected layer. The fully connected layer (also known as the dense layer) significantly plays a unique role in neural network architecture. Its key task consists in transforming the three-dimensional neuronal structure of the previous layers into a one-dimensional structure, a process usually found in convolutional neural networks or pooling layers, and is professionally known as “flattening”. These active neurons are capable of a high degree of information exchange, which greatly enhances the complexity of interactions between different features within the layer. In addition, they provide feasibility and convenience for subsequent classification or regression prediction tasks. The details are as follows:

$$x_j^l = f\left(\sum_{i_1=1}^{Height}\sum_{i_2=1}^{Width}\sum_{i_3=1}^{Channel} x_{i_1 i_2 i_3}^{l-1} W_{i_1 i_2 i_3}^{l} + b_j^l\right), j \in (1, J) \tag{26}$$

In the expression, x_j^l is the j neuron of the fully connected layer l. J is the layer size. $x_{i_1 l_2 i_3}^{l-1}$ is a neuron in the layer 3D feature map. $W_{l_1 i_2 i_3}^{l}$ is the weight corresponding to $x_{i_1 l_2 i_3}^{l-1}$ between $l-1$ layer and l layer. i_1, i_2, i_3 denote the height, width, and position of the channel, respectively. b_j^l is the bias of the input term x_j^l. $f(\cdot)$ is the activation function.

The high-level feature vectors derived from the fully connected layer will go into the Softmax layer, and this step is defined as:

$$y_k = \left[P(prediction = k \mid x^{l-1}; W_k^l)\right] = \frac{e^{W_k^l x^{l-1}}}{\Sigma_{m=1}^{K} e^{W_k^l x^{l-1}}}, k \in (1, K) \tag{27}$$

$$x^{l-1} = \left[x_1^{l-1}, \ldots, x_i^{l-1}, \ldots, x_I^{l-1}\right]^T \tag{28}$$

$$W_k^l = \left[W_{k1}^l, \ldots, W_{ki}^l, \ldots, W_{kI}^l\right], W^l = \left[W_1^l, \ldots, W_k^l, \ldots, W_K^l\right]^T \tag{29}$$

When rating the categorization performance of a neural network, the error is often further investigated, which stems from the gap between the actual category of each sample and the discrete probability distribution of the expected categories. This error is often quantified in terms of cross entropy and is chosen as the objective function. Cross entropy can directly characterize the similarity between the predictions of the model and the real data. This method can effectively improve the classification accuracy of the model, so it is widely used in practice. Therefore, it is defined as:

$$E(W) = -\frac{1}{P}\left[\sum_{p=1}^{P}\sum_{k=1}^{K} 1\{L^P = k\} \log(y_k^p)\right] \tag{30}$$

$$E(W) = -\frac{1}{P}\left[\sum_{p=1}^{P}\sum_{k=1}^{K} 1\{L^P = k\} \log g\left(\frac{e^{[W_k^i x^{j-1}]^p}}{\sum_{m=1}^{K} e^{[W_k^i x^{j-1}]^p}}\right)\right] \tag{31}$$

In the expression, $E(W)$ is the objective function. P is the sample size. $1\{\cdot\}$ is the indicator function. y_k^p is the probability that the sample p is the kth class. L^P is the true label of the sample p. $[\cdot]^P$ is the matrix operation of the sample p.

In advancing scientific research experiments, the stochastic gradient descent method (SGDM) with momentum terms is often chosen to optimize the initial weights, which are randomly selected.

3. Bridge inspection data calculation and risk assessment results

3.1. Pre-processing of data

3.1.1. Denoising of wavelet packets. The wavelet packet method introduced earlier is utilized to denoise the signals obtained by sampling on the sensors, and the original signal waveform, time-frequency diagram, and spectrogram are shown in Fig. 1-Fig. 3, respectively. The db5 wavelet is used, the number of decomposition layers is 3, and SURE is chosen as the threshold selection criterion, and the results are shown in Fig. 4-Fig. 6. From Fig. 1-Fig. 3, it can be seen that the signal changes significantly after wavelet packet denoising. The time-domain waveform of the signal before denoising is interspersed with a large amount of white noise, which presents a large number of burrs in appearance. The time-frequency and spectrograms appear regular and uncluttered relative to the denoised signal.

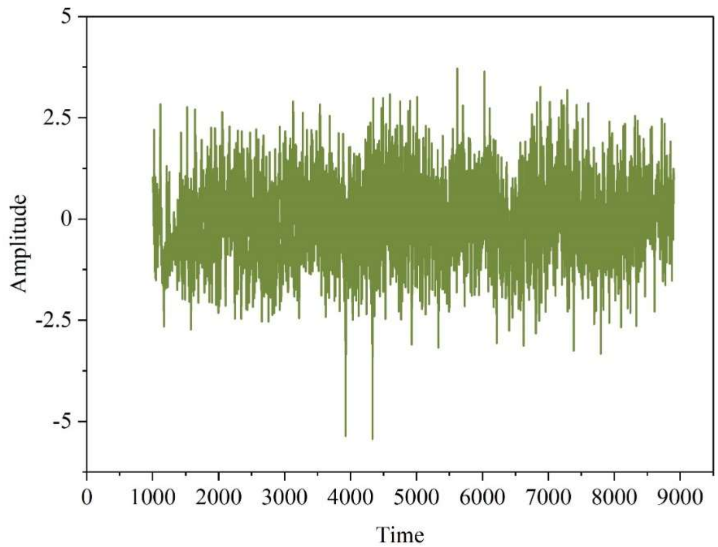

Fig. 1. Time domain graph

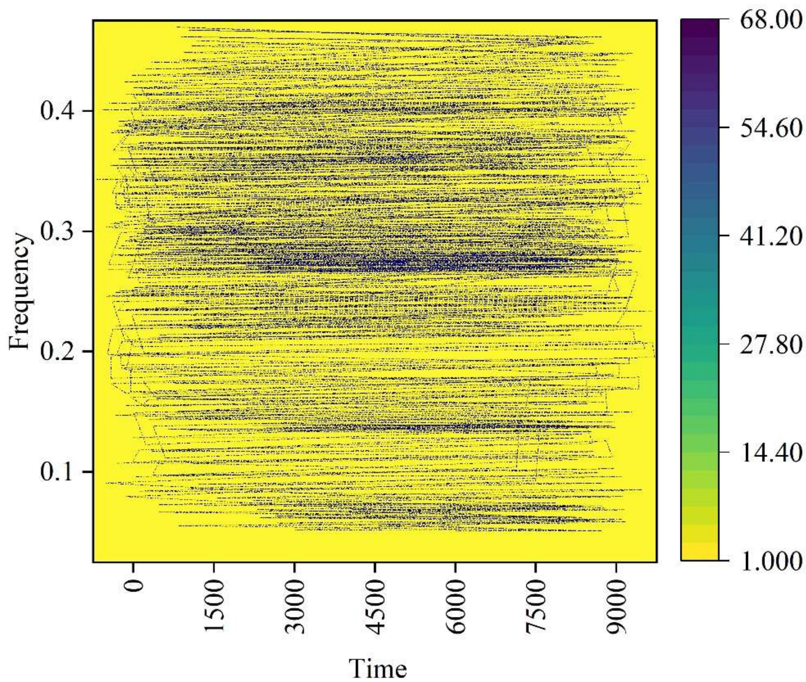

Fig. 2. Time frequency diagram

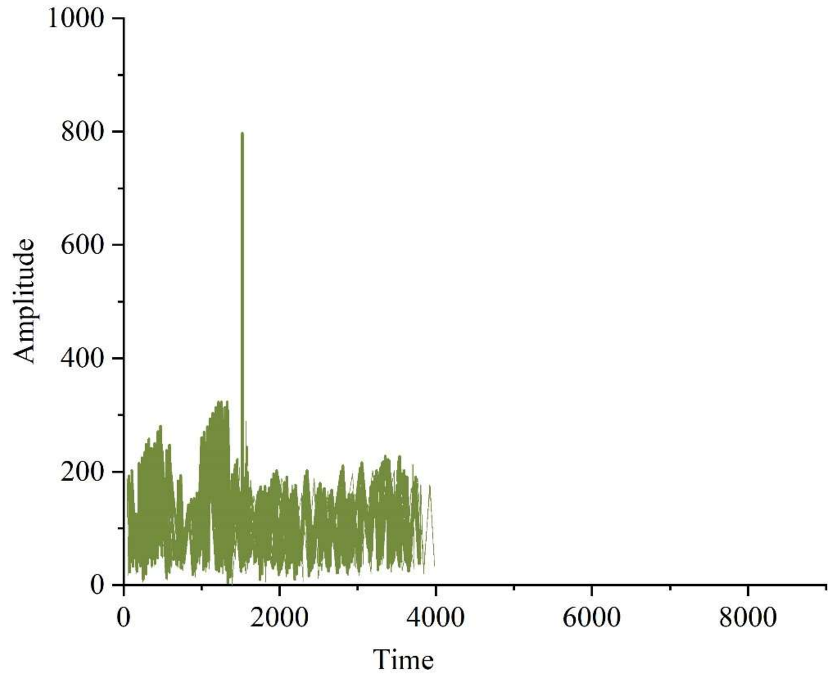

Fig. 3. Spectrogram

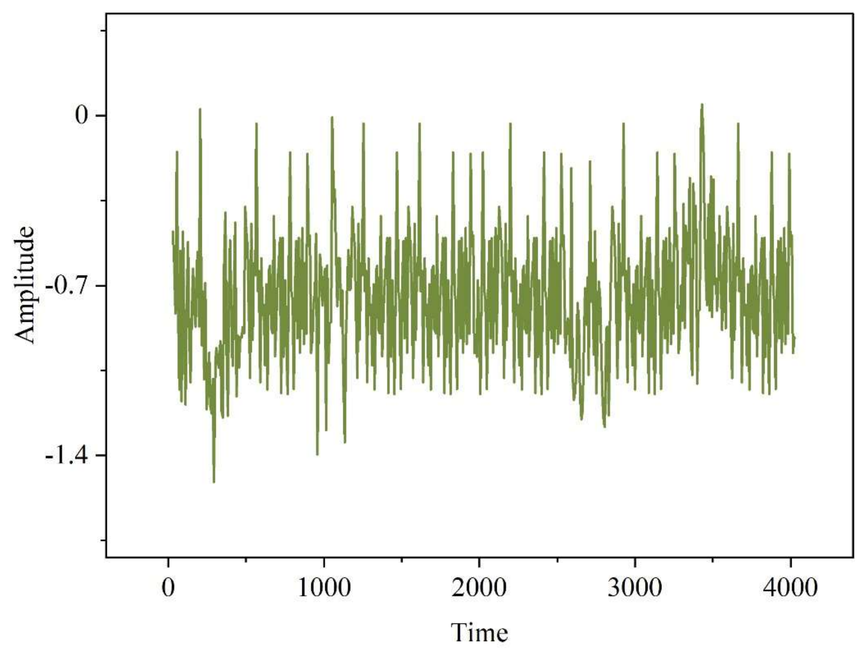

Fig. 4. Time domain graph

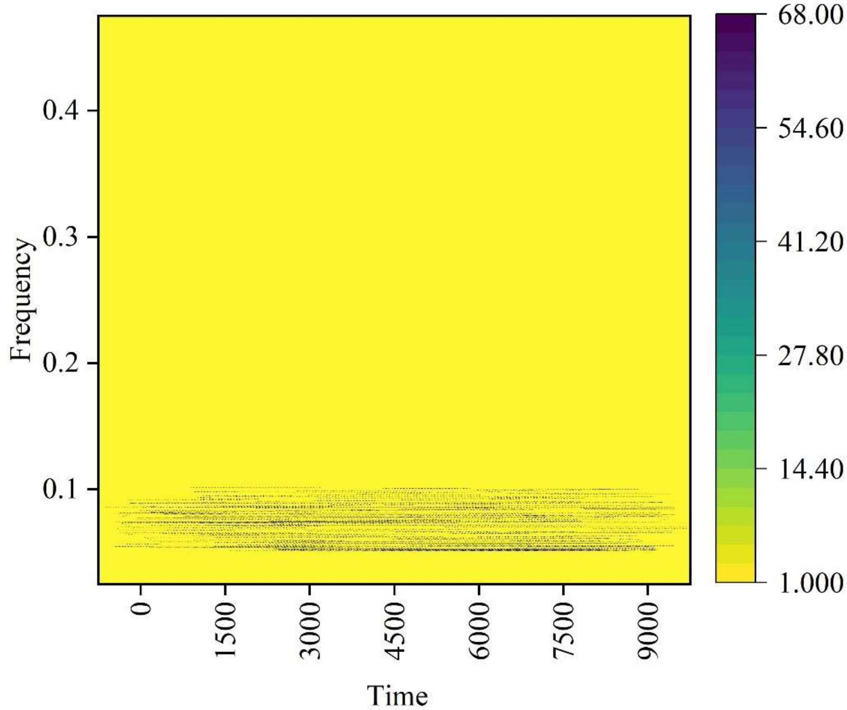

Fig. 5. Time frequency diagram

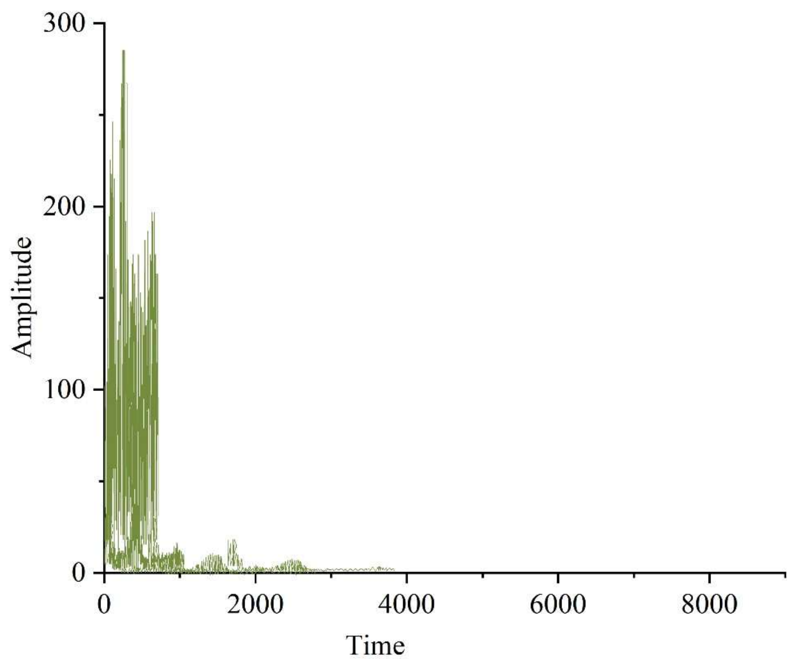

Fig. 6. Spectrogram

3.1.2. Hilbert transform processing. Then the Hilbert transform is applied to the noise reduced signal to obtain the corresponding analyzed signal. The analytic signal eliminates the negative frequencies on the one hand, and suppresses the cross terms generated by the Wigner distribution of the signal on the other hand.

3.2. Time-frequency plots and spectrograms of experimental signals

The vibration signal of a bridge satisfies the mechanical structure, and a healthy vibration signal is a low-frequency signal from the mechanical principle. When the bridge fails, its vibration becomes a signal with high frequencies interspersed, and the graph in the time domain looks like a lot of small imperfections. The high-frequency signal is its failure signal, at this time the spectrum of the vibration signal will change. For a healthy bridge vibration signal spectrum, should be the maximum amplitude at the fundamental frequency, octave at the amplitude of the gradual decline. And mixed with the fault signal spectrum will become irregular, and sometimes in the non-octave frequency at the larger amplitude. Of course, the Fourier transform is only a most basic fault signal analysis method, the Fourier transform can't pursue the high resolution of time domain and frequency domain at the same time, and its detail description is not intuitive. The Wigner-Ville distribution analyzes the signal by combining the information of the signal in time and frequency, and can visualize the information of the time-frequency characteristics of the signal. The vibration signals obtained from the bridge sensors were subjected to time-frequency analysis to observe the time-frequency information in three cases: no disease, slight disease, and disease. In the time-frequency diagram, from the location of the energy aggregation zone, if the energy aggregation zone is at the low frequency, it means that the signal is mainly low-frequency signal, then the health condition is good. If the energy aggregation area is at the middle and high frequencies, it indicates that the bridge is diseased. From the intensity point of view, if the intensity of the energy aggregation area is abnormally high, it means that the bridge is also diseased at this time, and this situation is further analyzed by combining with the frequency spectrum diagram. Through the time-frequency diagram in the location of the energy gathering area, intensity and signal Fourier transform frequency of the three combined with each other, and finally determine whether the bridge is diseased and the degree of disease.

The following three typical bridge vibration signals are selected from more than 2000 measured data. Observe the time-frequency diagrams and spectrograms of the vibration signals of bridge pavements from No. 1 to No. 3. The time-frequency diagrams and spectrograms of the vibration signals of bridge pavements from No. 1 to No. 3 are shown in Figs. 7-9, and Figs. (a) and (b) represent the time-frequency and spectrograms of vibration signals of bridge pavements, respectively.

No. 1 bridge energy aggregation area are in the low-frequency, and the energy intensity is small, the area is small, while the spectrum also meets the octave of the gradual attenuation, it can be judged that the group of signals are mainly low-frequency signals, the structural health of the group of bridges and pavements is good, there is no disease.

No. 2 Although the energy aggregation area is in the low-frequency band, the energy intensity is abnormally large, so the structural health of the No. 2 bridge pavement also belongs to the slight disease.

Observing the time-frequency diagram of the vibration signal of the bridge surface of No. 3, it can be seen that the energy aggregation area has an unusually large intensity, and it is almost spread over the whole frequency band, so the structural health of the bridge pavement in this group belongs to the disease.

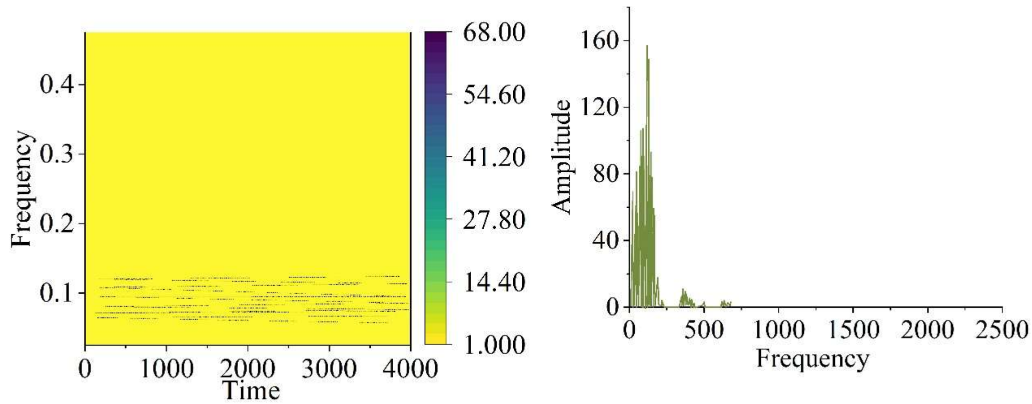

(a)Time frequency diagram (b)spectrogram

Fig. 7. Time frequency diagram and spectrum diagram of bridge one

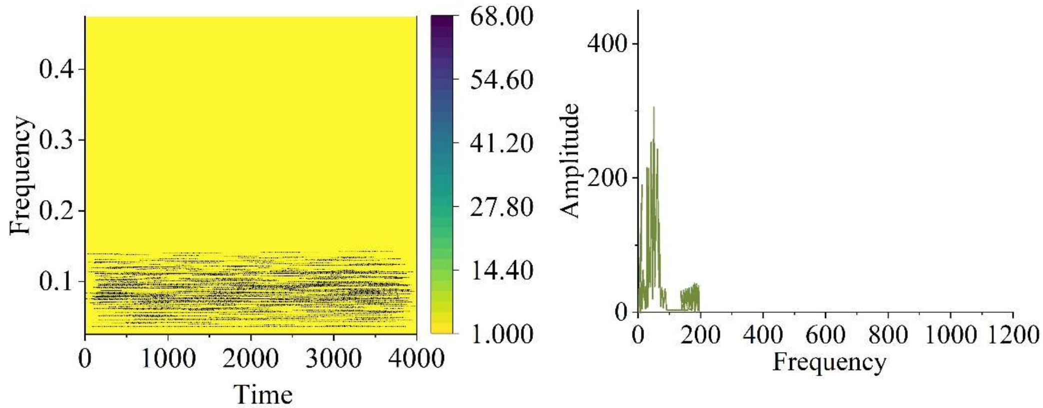

(a)Time frequency diagram (b)spectrogram

Fig. 8. Time frequency diagram and spectrum diagram of bridge two

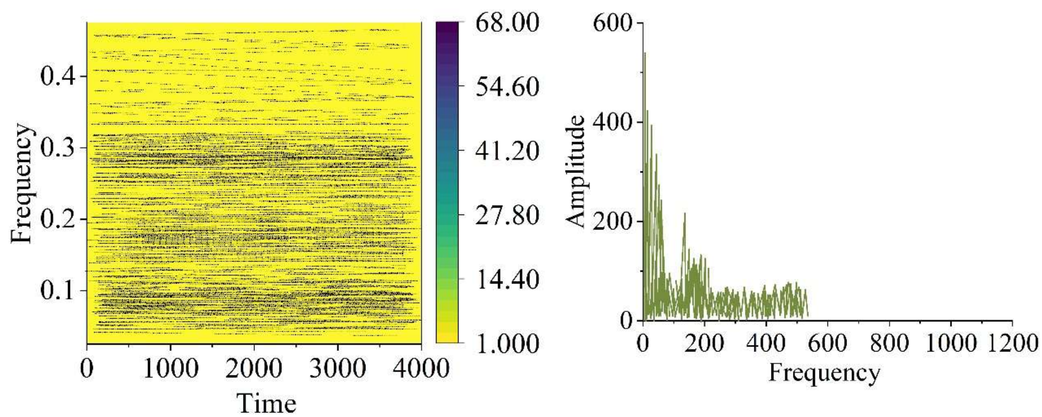

(a)Time frequency diagram (b)spectrogram

Fig. 9. Time frequency diagram and spectrum diagram of bridge three

3.3. Analysis of risk assessment results

The samples in the training and validation sets are screened out, and the set composed of the remaining samples is the test set for this experiment, which is used to simulate the real situation of a large number of bridge structural health monitoring data. The trained network model was tested on the test set containing 18000 wavelet time-frequency maps, and the test results are shown in Fig. 10, where the numbers 1-7 represent seven monitoring data types: normal, missing, sub-minor, outlier, over-range oscillation, trend and drift, respectively. Among them, there are 17600 pictures classified accurately and 352 pictures classified incorrectly, with a recognition accuracy of 97.78% and a total time of 56.25 s. The experimental results show that the convolutional neural network based on the information in the time-frequency domain has the advantages of high accuracy and fast computation speed.

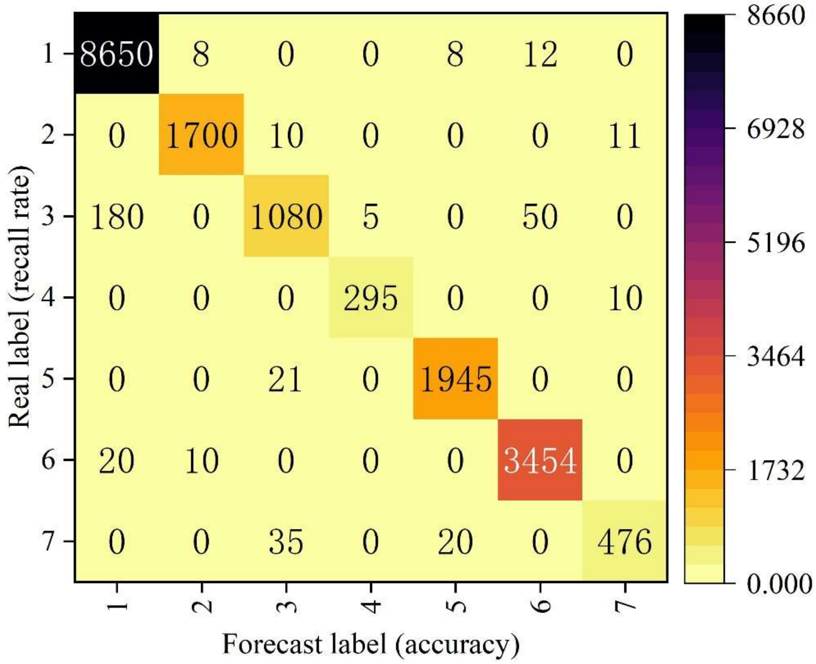

Fig. 10. Test set confusion matrix

A summary of the F1 scores and accuracies for data distortion detection on the test set is shown in Table 1, where the value for each category is F1score (%), and the total refers to the number of correctly identified samples as a percentage of all samples. 7 data types achieved high F1 scores on the test set, with the "missing" type achieving the highest score of 99.98%. For the "drift" type in Case 2 and Case 3, the accuracy is improved by 18.99% and 22.78%, respectively, compared to Case 1. The outliers are improved by 4.97% and 4.50% respectively, while the rest of the types are not improved much. From the above results, it can be seen that the accuracy of the convolutional neural network model increases gradually with the increase of the number of samples in the training and validation sets.

Table 1. The test set is distorted to detect f1 scores and accuracy

Data type	1	2	3
Normal	98.43	98.72	99.06
Deletion	99.52	99.65	99.98
Subfraction	91.34	92.93	95.92
Dispersion value	74.23	79.20	78.73
Overflow shock	99.39	99.11	99.37
Trend	95.17	97.66	98.3
Drift	64.77	83.76	87.55
Total	96.16	97.61	98.13

Although the accuracy of the test set for each case is more than 96%, the F1 scores for “outliers” and “drift” do not exceed 90%, and the precision is higher than the recall for all cases except case 3 for outliers, and the recall and precision for these three categories are shown in Table 2. The recall and precision rates of these three categories are shown in Table 2.

Table 2. Performance assessment of "drift" and "drift" test sets

Data type	Dispersion value			Drift		
	1	2	3	1	2	3
Recall rate	72.69	76.43	86.18	61.01	79.26	85.93
Precision rate	75.78	82.13	72.51	69.11	88.77	89.30

Table 3 shows the number of data of each type in the test set. The "normal" sample size is 29.5 times that of the "outlier", while the "drift" sample size is about one-seventh of the "trend".

Table 3. Test the number and proportion of each type of data

Monitor data type	Quantity	
	Test result	Actual situation
Normal	8678	8850
Deletion	1721	1718
Subfraction	1615	1146
Dispersion value	305	300
Overflow shock	1966	1973
Trend	3484	3516
Drift	531	497
Distorted data	9622	9150
Total data	18000	/

The distribution of the monitoring data of each sensor reflects the cumulative total amount of each monitoring data at different times, this paper shows the distribution of the monitoring data of some sensors, the data distribution of sensors 1-4 is shown in Figures 11 to 14, and the Y-axis numbers 1-7 represent seven different data types such as normal, missing, sub-small, outliers, overrange oscillations, trends and drifts. From the figure it can be seen that neighboring sensors not only have similar data quality, but also are similar in the distribution of distorted data types and the sequence of their temporal development. A large amount of over-range oscillation data appears in sensors 1-4 for almost the whole month, during which the sensors may have defects of their own leading to their accuracy degradation.

The data calculation and risk assessment method proposed in this paper can not only significantly reduce the number of false alarms caused by distortions in the bridge structural health monitoring system, but also the above information can provide theoretical guidance for the next stage of repairing the bridge monitoring data as well as the maintenance of the structural health monitoring system. In this paper, the diagnosis of the monitoring data on the computer takes about 2 hours, and the accuracy rate reaches more than 97%, which is an efficient and accurate data calculation and risk assessment method compared with the traditional manual inspection.

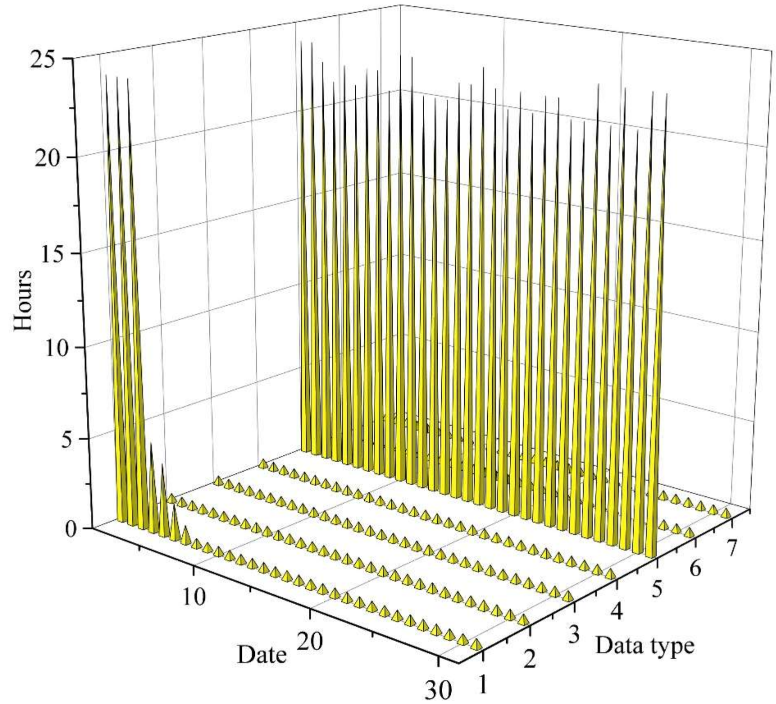

Fig. 11. Sensor 1 monitoring data distribution

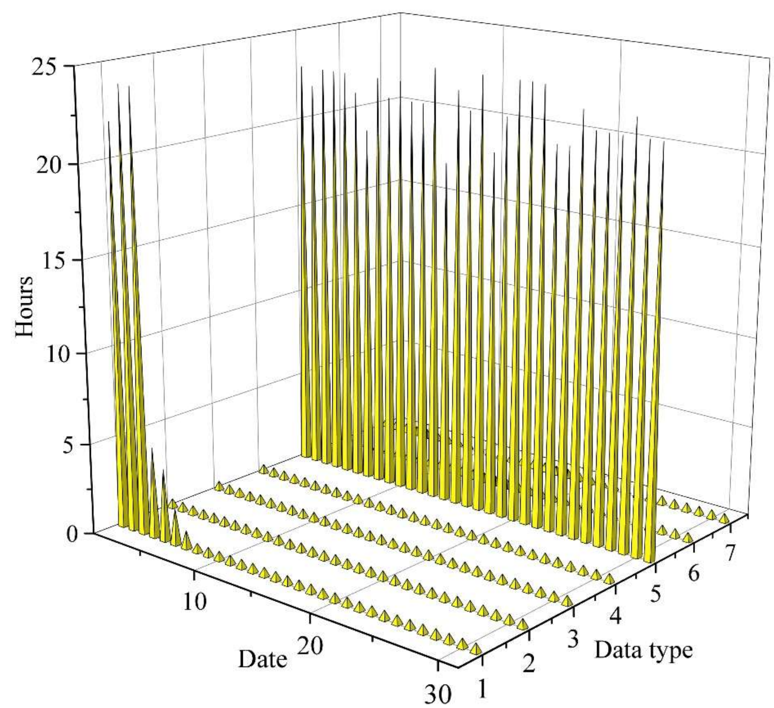

Fig. 12. Sensor 2 monitoring data distribution

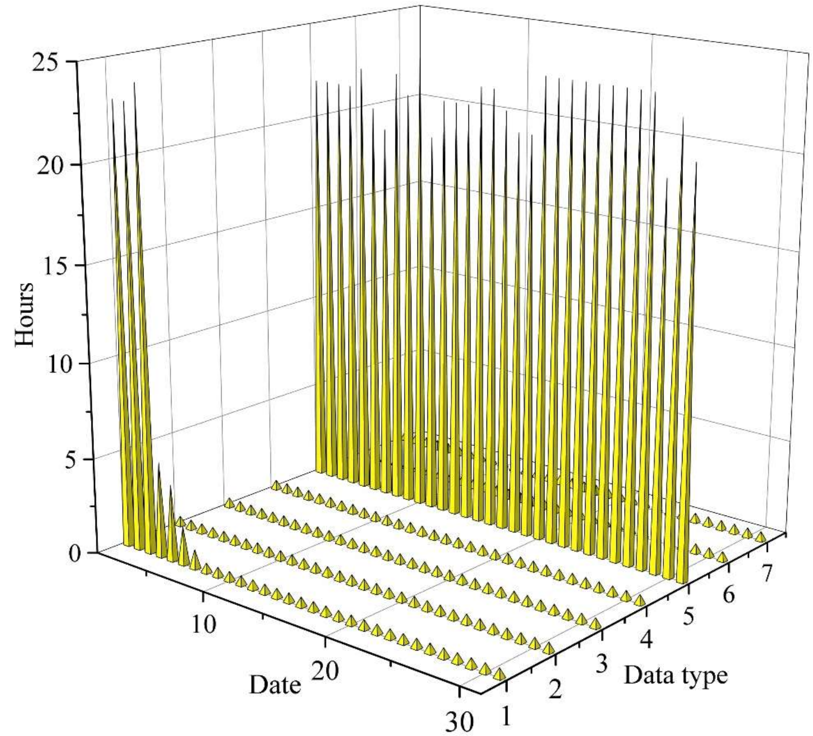

Fig. 13. Sensor 3 monitoring data distribution

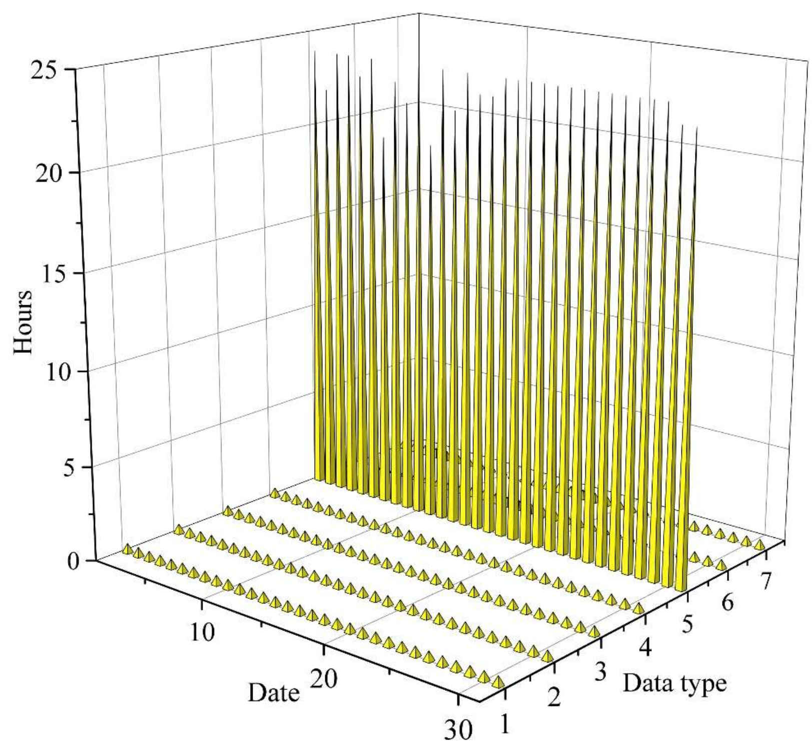

Fig. 14. Sensor 4 monitoring data distribution

4. Conclusion

This paper proposes a bridge inspection data calculation and risk assessment method that integrates time domain and frequency domain information with convolutional neural network as the basic architecture.

In this paper, wavelet packet denoising and pre-processing of bridge vibration signals are carried out to obtain more regular and uncluttered signals. The time-frequency diagram and spectrogram data analysis was made for bridges No. 1 to No. 3, No. 1 bridge energy aggregation area is at low frequency, energy intensity is small, area is small, the spectral octave shows the law of gradual attenuation, the structural health of this group of bridges is good, there is no disease. The energy gathering area of bridge No. 2 is at low frequency, but its energy intensity is large, and the bridge pavement structure belongs to slight disease. Observing bridge No. 3, it is found that the intensity of its energy aggregation area is abnormally large and occupies the whole frequency band, so the structural health of bridge No. 3 belongs to disease. This result shows that the method of this paper is able to analyze the time-frequency information of bridges in different health conditions and make accurate data analysis.

The monitoring data type identification accuracy of this paper's model is 97.78%, and it can obtain the distribution number of abnormal data sites and analyze the distribution of sensor abnormal data according to the risk assessment results, so that the distribution of abnormal data of bridge monitoring data can be obtained more fully and comprehensively. The total time for testing 18000 wavelet time-frequency maps is 56.25s, and the detection effect is better than the traditional methods such as manual detection, which provides a new research idea for the field of bridge detection data calculation and risk assessment.

References

[1] Lak, A., Ramezani, M., & Aghamolaei, R. (2019). Reviving the lost spaces under urban highways and bridges: an empirical study. Journal of Place Management and Development, 12(4), 469-484.

[2] Zabalueva, T. R., & Zakharov, A. V. (2020, April). Building-Bridges and Building-Platforms as Impact Into Sustainable Development of City Architecture. In IOP Conference Series: Earth and Environmental Science (Vol. 459, No. 5, p. 052025). IOP Publishing.

[3] Huang, M., Lei, Y., Li, X., & Gu, J. (2021). Damage identification of bridge structures considering temperature variations-based SVM and MFO. Journal of Aerospace Engineering, 34(2), 04020113.

[4] Yoon, S., Spencer Jr, B. F., Lee, S., Jung, H. J., & Kim, I. H. (2022). A novel approach to assess the seismic performance of deteriorated bridge structures by employing UAV-based damage detection. Structural Control and Health Monitoring, 29(7), e2964.

[5] An, Y., Chatzi, E., Sim, S. H., Laflamme, S., Blachowski, B., & Ou, J. (2019). Recent progress and future trends on damage identification methods for bridge structures. Structural Control and Health Monitoring, 26(10), e2416.

[6] Karimi, S., & Mirza, O. (2023). Damage identification in bridge structures: review of available methods and case studies. Australian Journal of Structural Engineering, 24(2), 89-119.

[7] Tefera, B., Zekaria, A., & Gebre, A. (2023). Challenges in applying vibration-based damage detection to highway bridge structures. Asian Journal of Civil Engineering, 24(6), 1875-1894.

[8] Abdallah, A. M., Atadero, R. A., & Ozbek, M. E. (2022). A state-of-the-art review of bridge inspection planning: Current situation and future needs. Journal of Bridge Engineering, 27(2), 03121001.

[9] Luo, K., Kong, X., Zhang, J., Hu, J., Li, J., & Tang, H. (2023). Computer vision-based bridge inspection and monitoring: A review. Sensors, 23(18), 7863.

[10] Dorafshan, S., & Maguire, M. (2018). Bridge inspection: Human performance, unmanned aerial systems and automation. Journal of Civil Structural Health Monitoring, 8, 443-476.

[11] Turksezer, Z. I., Iacovino, C., Giordano, P. F., & Limongelli, M. P. (2021). Development and implementation of indicators to assess bridge inspection practices. Journal of Construction Engineering and Management, 147(12), 04021165.

[12] Dorafshan, S., Maguire, M., Hoffer, N. V., & Coopmans, C. (2017, June). Challenges in bridge inspection using small unmanned aerial systems: Results and lessons learned. In 2017 international conference on unmanned aircraft systems (ICUAS) (pp. 1722-1730). IEEE.

[13] Quirk, L., Matos, J., Murphy, J., & Pakrashi, V. (2018). Visual inspection and bridge management. Structure and Infrastructure Engineering, 14(3), 320-332.

[14] Bertola, N. J., & Brühwiler, E. (2023). Risk-based methodology to assess bridge condition based on visual inspection. Structure and Infrastructure Engineering, 19(4), 575-588.

[15] Zakaria, M., Karaaslan, E., & Catbas, F. N. (2022). Advanced bridge visual inspection using real-time machine learning in edge devices. Advances in Bridge Engineering, 3(1), 27.

[16] Fang, C., Xu, Y. L., Hu, R., & Huang, Z. (2022). A web‐based and design‐oriented structural health evaluation system for long‐span bridges with structural health monitoring system. Structural Control and Health Monitoring, 29(2), e2879.

[17] Campbell, L. E., Connor, R. J., Whitehead, J. M., & Washer, G. A. (2020). Benchmark for evaluating performance in visual inspection of fatigue cracking in steel bridges. Journal of Bridge Engineering, 25(1), 04019128.

[18] Rakoczy, A. M., Ribeiro, D., Hoskere, V., Narazaki, Y., Olaszek, P., Karwowski, W., ... & Schmidt, F. (2024). Technologies and Platforms for Remote and Autonomous Bridge Inspection–Review. Structural Engineering International, 1-23.

[19] Ivanovic, A., Markovic, L., Car, M., Duvnjak, I., & Orsag, M. (2021). Towards autonomous bridge inspection: Sensor mounting using aerial manipulators. Applied Sciences, 11(18), 8279.

[20] Nasimi, R., Moreu, F., & Fricke, G. M. (2023). Sensor equipped UAS for non-contact bridge inspections: field application. Sensors, 23(1), 470.

[21] Wang, R., & Kawamura, Y. (2016). An automated sensing system for steel bridge inspection using GMR sensor array and magnetic wheels of climbing robot. Journal of Sensors, 2016(1), 8121678.

[22] Kakillioglu, B., Wang, J., Velipasalar, S., Janani, A., & Koch, E. (2019, November). 3D sensor-based UAV localization for bridge inspection. In 2019 53rd Asilomar Conference on Signals, Systems, and Computers (pp. 1926-1930). IEEE.

[23] Zulifqar, A., Cabieses, M., Mikhail, A., & Khan, N. (2014). Design of a bridge inspection system (BIS) to reduce time and cost. George Mason University: Farifax, VA, USA.

[24] Comisu, C. C., Taranu, N., Boaca, G., & Scutaru, M. C. (2017). Structural health monitoring system of bridges. Procedia engineering, 199, 2054-2059.

[25] Zhu, Y. F., Ren, W. X., & Wang, Y. F. (2022). Structural health monitoring on Yangluo Yangtze River Bridge: implementation and demonstration. Advances in Structural Engineering, 25(7), 1431-1448.

[26] Wang, H., Tao, T., Li, A., & Zhang, Y. (2016). Structural health monitoring system for Sutong cable-stayed bridge. Smart structures and systems, 18(2), 317-334.

[27] Sun, Z., Zou, Z., & Zhang, Y. (2017). Utilization of structural health monitoring in long‐span bridges: case studies. Structural Control and Health Monitoring, 24(10), e1979.

[28] Saidin, S. S., Jamadin, A., Abdul Kudus, S., Mohd Amin, N., & Anuar, M. A. (2022). An overview: The application of vibration-based techniques in bridge structural health monitoring. International Journal of Concrete Structures and Materials, 16(1), 69.

[29] Ye, S., Lai, X., Bartoli, I., & Aktan, A. E. (2020). Technology for condition and performance evaluation of highway bridges. Journal of Civil Structural Health Monitoring, 10, 573-594.

[30] Sun, Z., & Sun, H. (2018). Jiangyin Bridge: An example of integrating structural health monitoring with bridge maintenance. Structural Engineering International, 28(3), 353-356.

[31] Tuna Alikaşifoğlu,Bünyamin Kartal,Eray Özgünay & Aykut Koç. (2025). Joint time-vertex fractional Fourier transform. Signal Processing,233,109944-109944.

[32] Henry Ruiz Guzman,Tyler Adams,Afolabi Agbona,Matthew Wolfe,Mark Everett,Jean Francois Chamberland & Dirk B. Hays. (2025). Thresholding and continuous wavelet transform (CWT) analysis of Ground Penetrating Radar (GPR) data for estimation of potato biomass. Computers and Electronics in Agriculture,232,110114-110114.

[33] Muharrem Çelebi,Sıtkı Öztürk & Kaplan Kaplan. (2025). An enhanced deep learning model based on smoothed pseudo Wigner-Ville distribution technique for emotion recognition with channel selection. Ain Shams Engineering Journal,16(2),103264-103264.

[34] Carlo Ciulla. (2025). Two-dimensional image noise removal and reconstruction using discrete Fourier transform, k-space filtering and Z-space filtering. Progress in Engineering Science,2(1),100056-100056.